LSTM-Based Time-Frequency Domain Channel Estimation for OTFS Modulation

Ana Flavia dos Reis, Bruno Sens Chang, Yahia Medjahdi, Glauber Brante, Faouzi Bader

LSTM-Based Time-Frequency Domain Channel Estimation for OTFS Modulation

Ana Flávia dos Reis, Bruno Sens Chang, *Member, IEEE*, Yahia Medjahdi, *Member, IEEE*, Glauber Brante, *Senior Member, IEEE* and Faouzi Bader, *Senior Member, IEEE*

***Abstract*—Orthogonal Time Frequency Space (OTFS) is a promising modulation scheme that works in the delay-Doppler (DD) domain, offering resistance to frequency selective fading and time-varying channels. Thus, OTFS channel estimation assumes great significance for successful transmission. Typically, it requires allocating pilots in the DD domain, which often results in an increase in the peak-to-average power ratio (PAPR) and high complexity to detect the received signal. In response to these issues, we present a solution that estimates the channel in the time-frequency (TF) domain. In addition, although several works in the literature present solutions for OTFS channel estimation, few consider the presence of high-power amplifiers (HPAs) and explain the impact of nonlinear effects on channel estimation and system performance. Starting from channel estimation based on preambles and pilots in the TF domain, we present a solution capable of obtaining reliable channel estimation using a long short-term memory (LSTM) network in highly selective channel conditions, effectively compensating for nonlinearities in signal reception. Our results validate the effectiveness of the proposed solution, highlighting its potential to improve the performance and robustness of OTFS communication systems in real scenarios with nonlinear HPA effects.**

***Index Terms*—Channel estimation, LSTM, OTFS, HPA distortions, Vehicular communication.**

I. Introduction

MEETING the increasing demand for higher data rates, reliability, and connectivity, the dynamic scenario of modern wireless communication systems poses significant challenges [1]. In particular, vehicular communication is one of the areas of greatest interest for the development of solutions within future 6G applications, where one of the challenges is to estimate the wireless channel with sufficient quality in order to ensure reliable communication.

As vehicular communication scenarios continue to evolve, the demand for robust and efficient wireless communication systems becomes increasingly critical. In this context, although widely adopted, conventional multicarrier transmission schemes, such as orthogonal frequency division multiplexing (OFDM) modulation, reveal inherent limitations that may impair their effectiveness in future vehicular environments [2]. The sensitivity of OFDM to inter-carrier interference (ICI) and its vulnerability to time-varying channels and frequency selectivity [3], particularly in high-mobility scenarios, highlight the importance of re-evaluating its suitability for future vehicle communication systems.

In response to this, Orthogonal Time Frequency Space (OTFS) [4], [5] has emerged as a promising modulation scheme, presenting a new approach to wireless communication. Unlike traditional modulation methods, OTFS uses the delay-Doppler (DD) domain to encode and transmit information, making it robust to the doubly selective channel effects. The OTFS addresses the limitations of conventional communication systems in dynamic and highly dispersive environments. In addition, the ability of OTFS to mitigate ICI and effectively handle time-varying channels opens up new possibilities for communication technologies, being particularly suitable for high mobility scenarios and holding the promise of improved performance and extended applications in modern wireless communication systems.

In this context, channel estimation in OTFS communication systems is critically important, as it significantly affects the overall system performance and unlocks the full potential of this state-of-the-art technology. Most of the existing estimation techniques for OTFS are based on the DD domain pilot-adding method [6], [7]. A well-known OTFS channel estimation approach in the literature is presented in [6], in which the authors propose a threshold-based estimation technique that considers an OTFS frame with embedded pilots, that is surrounded by a guard band to avoid interference with the data symbols. Another work, presented in [7], also considers DD-embedded pilots along with data symbols, where a cross-correlation-based algorithm is presented to perform Doppler domain channel estimation. It is highlighted that the guard band insertion significantly degrades the spectral efficiency.

As analytically characterized by [8], although OTFS signals can exhibit lower peak-to-average power ratio (PAPR) compared to OFDM, the issue of high PAPR persists in such systems, posing a significant challenge in OTFS channel estimation. The high PAPR values can lead to nonlinear distortions in the presence of high power amplifiers (HPA), degrading the overall system performance. Consequently, researchers have dedicated several efforts to develop PAPR reduction techniques

This work was partially supported by Coordenação de Aperfeiçoamento de Pessoal de Nível Superior – Brasil (CAPES) – Finance Code 001, the Conselho Nacional de Desenvolvimento Científico e Tecnológico (CNPq), under grants 307226/2021-2 and 402378/2021-0, INESC P&D Brazil, and the Institut Supérieur d'Électronique de Paris (ISEP). Ana Flávia dos Reis is with the Instituto Nacional de Telecomunicações (INATEL), Santa Rita do Sapucaí, Brazil (ana.reis@posdoc.inatel.br). Bruno Sens Chang and Glauber Brante are with the Federal University of Technology - Paraná (UTFPR), Curitiba, Brazil ({bschang, gbrante}@utfpr.edu.br). Yahia Medjahdi is with the IMT Nord Europe, Institut Mines-Télécom, Univ. Lille, Centre for Digital Systems, Lille, France (yahia.medjahdi@imt-nord-europe.fr). Faouzi Bader is with the Technology Innovation Institute, Masdar City, Abu Dhabi, United Arab Emirates (carlos-faouzi.bader@tii.ae).

for OTFS [9], [10].

Nonetheless, it is important to highlight that research regarding the influence of high PAPR on channel estimation is still incipient in the OTFS literature. Works such as [6], [7] assume a linear communication environment, where an ideal radio frequency (RF) interface is considered. In this simplified model, the channel response is considered to be linear and time-invariant, overlooking potential nonlinear distortions that practical components may introduce. However, in real-world communication systems, nonlinearities in the RF interface can have a significant impact on the estimation of the OTFS channel and, consequently, the overall performance of the communication system. Addressing these nonlinear effects will be crucial in developing robust and high-performance OTFS channel estimators. Furthermore, the analysis made in [9] and [11] highlights that the addition of pilot structures with high power in the DD domain can induce a high PAPR. Consequently, this increase in PAPR renders these estimators impractical [12].

The work in [13] is an important reference for learning methods on OFDM channel estimation, being the first to present that offline-trained deep learning models can be successfully employed to estimate channels impaired with nonlinear distortions. In the OTFS context, different methods are presented in the literature to reduce the PAPR when considering pilot placement in the DD domain. The work in [9], for example, proposes an iterative clipping and filtering method in a system with the pilots embedded in the DD domain, while [14] introduces a superimposed pilot placement scheme in the DD domain in conjunction with a discrete Fourier transform (DFT) propagation and [15] uses a deep learning architecture based on autoencoder to tackle the high PAPR. Although recognizing the existence of these methods of reducing PAPR, we emphasize that the primary focus of this paper is not on overall PAPR reduction. Therefore, we do not specifically address additional methods to mitigate PAPR. Instead, our focus is on developing a channel estimation method that effectively addresses the challenges posed by nonlinear distortions induced by HPAs, ultimately leading to improved accuracy in channel estimation for OTFS systems.

In this sense, different methods for OTFS channel estimation with the pilot transmission done in the time-frequency (TF) domain can be found, *e.g.*, in [11], [16]. Although the proposal in [16] results in a significant reduction in pilot overhead and an increase in bandwidth efficiency, it comes at the cost of high computational complexity, as it considers that while pilots are transmitted in the TF domain, another OTFS frame is needed to send the data. On the other hand, in [11], the advantages of reducing interference between pilots and data are achieved through the successive interference cancellation method. Another recent work in [17] proposes a low-overhead OTFS transmission scheme based on TF-domain pilot positioning. Here, we emphasize that these proposals are advantageous for reducing PAPR, however, these approaches offer less flexibility and adaptability compared to methods based on neural networks (NNs), and can entail higher computational complexity.

In this paper, we address channel estimation in OTFS systems considering HPA-induced nonlinearities. To this end, we propose a novel method based on TF domain channel estimation, reducing the PAPR while improving the capacity to detect OTFS signals. Starting with an initial coarse preamble-based estimate of the channel and using frequency domain pilots, we show that it is possible to reduce the pilot overhead and obtain a reliable channel estimate through a long short-term memory (LSTM) network, particularly in the presence of highly selective channels. Moreover, inspired by our previous research findings [18], which concentrated on the OFDM channel and capitalized on the generalization capability of LSTM-based deep learning architecture, we show that it is possible to obtain a channel estimate robust against nonlinear effects from HPA without requiring signal linearization at the transmitter. Then, we effectively compensate for the nonlinearities along with the channel estimation. It is important to note that the proposed method is specifically tailored for Symplectic Finite Fourier Transform (SFFT)-based OTFS systems, which leverage the OTFS compatibility with OFDM. Thus, the OTFS offers enhanced robustness in rapidly changing channels and can effectively handle large Doppler shifts, making it particularly well-suited for dynamic vehicular communication scenarios where mobility and channel variability are prominent factors. In contrast, OFDM is impaired in extreme scenarios [2]. To validate the efficacy of our proposed estimator, we conducted a comparative analysis against the classic methods outlined in prior works [6], [7]. Our method not only showcases enhanced precision in channel estimation, demonstrated through improved bit error rate (BER) and PAPR performances, but it also introduces a more efficient approach for OTFS communication systems within real-world scenarios. This is highlighted by a significant reduction in the computational complexity required for detecting the received signals compared to the benchmark methods.

The remainder of this paper is organized as follows. Section II presents the system model, including the implementation for OTFS transmission and the main characteristics of the HPA nonlinear distortion model. The benchmark OTFS channel estimation schemes are described in Section III, while the proposed LSTM-based channel estimator is detailed in Section IV. Results and discussions are presented in Section V and Section VI concludes the paper.

Notations: The notation $(\cdot)^{\dagger}$ indicates the conjugate operation, $*$ denotes the convolution, $(\cdot)_{\mathrm{M}}$ is the modulo operator of divider M, $(\cdot)^{\mathrm{H}}$ is the Hermitian and $\odot$ is the Hadamard product.

II. System Model

The most popular implementations for OTFS systems found in the literature use either the SFFT combined with a multicarrier modulation or the discrete Zak transform [3]. In this section, we first review the OTFS modulation implementation considered in this paper, where the inverse SFFT (ISFFT) and SFFT operations are used to convert time-varying channels into invariant channels in the DD domain and vice versa, allowing us to interpret the OTFS system as pre- and post-processing blocks applied to a multicarrier signaling scheme.

Subsequently, we describe the main attributes of the adopted HPA nonlinear distortion model.

A. OTFS Transmitter

Let us consider that the TF plane is sampled in time and frequency axes at intervals of T (seconds) and Δf (Hz), respectively. The multicarrier system is characterized as a block structure consisting of N symbols with M subcarriers each. As illustrated in Figure 1, the DD domain symbols, denoted as $X_{\mathrm{DD}}[l,k]$, are mapped to the two-dimensional DD grid, where $l \in \{0,\ldots,M-1\}$ is the delay index and $k \in \{0,\ldots,N-1\}$ is the Doppler index. As a key component in OTFS modulation, the SFFT operation enables efficient signal mapping between DD and TF domains. Thus, the M-by-N matrix of TF domain symbols is obtained via the ISFFT as

$$X_{\mathrm{TF}}[m,n] = \frac{1}{\sqrt{NM}} \sum_{k=0}^{N-1} \sum_{l=0}^{M-1} X_{\mathrm{DD}}[l,k] e^{j2\pi\left(\frac{nk}{N} - \frac{ml}{M}\right)}, \quad (1)$$

where the $m \in \{0,\ldots,M-1\}$ is the subcarrier index and $n \in \{0,\ldots,N-1\}$ is the symbol index.

The multicarrier modulation is performed on $X_{\mathrm{TF}}[m,n]$ to obtain the OTFS transmit signal $s(t)$ as

$$s(t) = \sum_{n=0}^{N-1} \sum_{m=0}^{M-1} X_{\mathrm{TF}}[m,n] g_{\mathrm{tx}}\left(t - nT\right) e^{j2\pi m\Delta f(t-nT)}, \quad (2)$$

where $g_{\mathrm{tx}}(t)$ is the pulse shape filter at the transmitter side. This operation is known as the Heisenberg transform, which describes a generalization of the OFDM transform, converting the TF-modulated signal into the time domain for transmission [4]. Finally, following a pattern similar to OFDM, a cyclic prefix (CP) is appended at the beginning of each symbol before being transmitted.

1) HPA Distortion Model

For a more realistic characterization of wireless communication scenarios, our analysis considers that this time-domain signal is affected by HPA-induced nonlinearities. The model of the HPA nonlinear distortions in the transmitted signal $s_{\mathrm{NLD}}(t)$ follows the memoryless HPA description in [19]. Such a model characterizes both amplitude to amplitude (AM/AM) and amplitude to phase (AM/PM) distortions, while it fits a commercial evaluation of HPA from the 3GPP [20] into a polynomial. This model shows that the HPA response is usually constant over the useful signal frequency band, allowing us to neglect the memory effect of the HPA on the channel. In addition, we assume that phase compensation is perfectly done at the receiver [21].

The key component in this modeling is Bussgang's Theorem [22], which states that if the input signal to the HPA has a Gaussian distribution, the output signal can be written as

$$\tilde{s}_{\mathrm{NLD}}(t) = \gamma_0 s(t) + \tilde{\mathfrak{D}}(t), \quad (3)$$

where $\tilde{\mathfrak{D}}(t)$ is a nonlinear distortion with zero mean and variance ${\sigma_{\tilde{\mathfrak{D}}}}^2$, that is uncorrelated with $s(t)$, while γ_0 describes a complex gain. Subsequently, as per the theorem, γ_0 is compensated at the transmitter and the output of the HPA is given by

$$s_{\mathrm{NLD}}(t) = s(t) + \mathfrak{D}(t), \quad (4)$$

where $\mathfrak{D}(t) = \tilde{\mathfrak{D}}(t)/\gamma_0$ is the residual nonlinear distortion induced by the HPA.

For the polynomial model description in [19], the relationship between the input signal $s(t)$ and amplified output signal $\tilde{s}_{\mathrm{NLD}}(t)$ can be expressed as

$$\begin{aligned} \tilde{s}_{\mathrm{NLD}}(t) &= \phi_a\big(\rho(t)\big) e^{j\left(\phi_p\left(\rho(t)\right)+\varphi(t)\right)} \\ &= \varsigma\big(\rho(t)\big) e^{j\varphi(t)}, \end{aligned} \quad (5)$$

in which $\phi_a\big(\rho(t)\big)$ and $\phi_p\big(\rho(t)\big)$ represent the AM/AM and AM/PM characteristics of the HPA, respectively, $\rho(t)$ is the input signal modulus and $\varphi(t)$ is the input signal phase. The complex soft envelope of the amplified output signal is

$$\varsigma\big(\rho(t)\big) = \phi_a\big(\rho(t)\big) e^{j\phi_p\left(\rho(t)\right)}, \quad (6)$$

which, according to [19], can be approximated as

$$\varsigma\left(\rho(t)\right) \approx \sum_{l=1}^{P} a_l \rho(t)^l, \quad (7)$$

in which a_l are the complex coefficients of the polynomial approximation, computed by using the least square (LS) method.

In order to reduce the nonlinear effects, the HPA is set to operate at a given Input Back-off (IBO) from its 1 dB compression point. In practice, this refers to the input power level at which the HPA performance drops by 1 dB from its linear response [23]. Consequently, prior to amplification through the HPA, the signal is scaled by using the gain

$$\varrho = \sqrt{\frac{\iota_{1\mathrm{dB}}}{10^{\frac{\mathrm{IBO}}{10}} \iota_s}}, \quad (8)$$

where $\iota_{1\mathrm{dB}}$ is the input power at 1 dB compression point and ι_s is the mean power of the input signal. This step ensures the targeted IBO level, maintaining the desired operating characteristics of the HPA.

B. Channel

The non-linearly amplified signal $s_{\mathrm{NLD}}(t)$ is then transmitted over a doubly selective channel being characterized by the delay-Doppler response [3]

$$h_{\mathrm{DD}}(\tau,\nu) = \sum_{\mathrm{K}=1}^{\kappa} h_{\mathrm{K}} \delta(\tau - \tau_{\mathrm{K}}) \delta(\nu - \nu_{\mathrm{K}}), \quad (9)$$

where τ and ν denote respectively delay and Doppler variables, $\kappa \in \mathbb{Z}$ is the number of resolvable propagation paths and $\delta(\cdot)$ is the Dirac delta function. Each path is represented by a $h_{\mathrm{K}} \in \mathbb{C}$ channel coefficient and has a delay $\tau_{\mathrm{K}} = \frac{l_{\tau_{\mathrm{K}}}}{M\Delta f}$ and Doppler frequency $\nu_{\mathrm{K}} = \frac{k_{v_{\mathrm{K}}} + \kappa_{v_{\mathrm{K}}}}{NT}$, where $l_{\tau_{\mathrm{K}}}$ and $k_{v_{\mathrm{K}}}$ represent the integer indices of the delay and Doppler bins and $\kappa_{v_{\mathrm{K}}}$ is the fractional Doppler. Fractional Doppler shifts are typical in high-mobility scenarios where significant relative velocity between the transmitter and receiver results in a more complex and varying frequency shift. This phenomenon is expected to

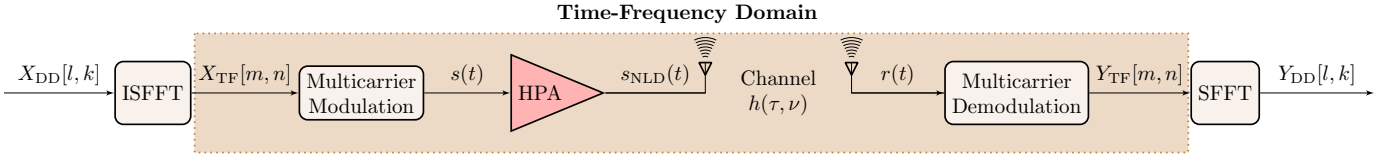

Fig. 1: SFFT-based OTFS architecture.

be prevalent in future vehicular communication systems. Thus, the discrete DD domain channel response $H_{\mathrm{DD}}[l,k]$ can be transformed to the TF domain using ISFFT as

$$\mathrm{H}_{\mathrm{TF}}[m,n] = \frac{1}{\sqrt{NM}} \sum_{k=0}^{N-1} \sum_{l=0}^{M-1} H_{\mathrm{DD}}[l,k] e^{j2\pi\left(\frac{nk}{N} - \frac{ml}{M}\right)}. \quad (10)$$

C. OTFS Receiver

The signal at the OTFS receiver is given by

$$r(t) = \int \int h_{\mathrm{DD}}(\tau,\nu) e^{j2\pi\nu(t-\tau)} s_{\mathrm{NLD}}(t-\tau) d\tau d\nu + w(t), \quad (11)$$

where $w(t) \sim \mathcal{N}(0,\sigma_w^2)$ is the additive white Gaussian noise (AWGN) in the time domain.

Next, the multicarrier demodulation of the received signal $r(t)$ is performed through the Wigner transform, which presents the inverse of the Heisenberg transform. Thus, the TF domain signal is obtained as

$$Y_{\mathrm{TF}}[m,n] = \int r(t) g_{\mathrm{rx}}^{\dagger}(t-nT)\, e^{-j2\pi m\Delta f(t-nT)} dt, \quad (12)$$

where $g_{\mathrm{rx}}^{\dagger}(t)$ represents the conjugate of the pulse shape filter at the receiver side. We consider the rectangular waveform for both $g_{\mathrm{tx}}(t)$ and $g_{\mathrm{rx}}(t)$ [24], [25]. By employing suitable equalization and decoding, the wireless communication channel can be effectively utilized for signal detection on the receiver side. Also, it is noted that the equalization process can be conducted in either TF or DD domains, in which the receivers in the DD domain often confers a higher degree of complexity. Referring to the details provided in [26], our system adopts the one-tap channel to derive the minimum mean square error (MMSE) equalizer within the TF domain. This equalizer is mathematically represented as follows

$$\mathrm{EQ}[m,n] = \frac{\mathrm{H}_{\mathrm{TF}}^{\dagger}[m,n]}{|\mathrm{H}_{\mathrm{TF}}[m,n]|^2 + \sigma_w^2}. \quad (13)$$

Thus, the received signal after equalization $\hat{X}_{\mathrm{TF}}[m,n]$ can be obtained as

$$\hat{X}_{\mathrm{TF}}[m,n] = Y_{\mathrm{TF}}[m,n]\mathrm{EQ}[m,n]. \quad (14)$$

Finally, the DD domain received signal is obtained by means of the SFFT operation, given by

$$Y_{\mathrm{DD}}[l,k] = \frac{1}{\sqrt{NM}} \sum_{n=0}^{N-1} \sum_{m=0}^{M-1} Y_{\mathrm{TF}}[m,n] e^{-j2\pi\left(\frac{kn}{N} - \frac{lm}{M}\right)}. \quad (15)$$

D. PAPR and HPA efficiency

Given the nonlinear characteristics of the HPA, the signal is subject to unnecessarily high power consumption due to possibly high PAPR, which may significantly damage the efficiency of the communication. The maximum PAPR for the input signal $s(t)$ is given by [8], [27]

$$\mathrm{PAPR} = \max_{t=\{0,1,\ldots,MN-1\}} \frac{|s(t)|^2}{P_{\mathrm{avg}}}, \quad (16)$$

where P_{avg} is average power of the signal over its entire duration T, given as

$$P_{\mathrm{avg}} = \frac{1}{T} \int_0^T |s(t)|^2 dt. \quad (17)$$

The complementary cumulative distribution function (CCDF) describes a signal's PAPR performance, analyzing its fluctuations' statistical behavior. The CCDF represents the probability that the PAPR exceeds a certain threshold, and it is mathematically expressed as

$$\mathrm{CCDF} = \mathbf{P}(\mathrm{PAPR} > \lambda) = 1 - \mathbf{P}(\mathrm{PAPR} \leq \lambda), \quad (18)$$

where λ is a constant and defines the threshold for the CCDF.

It is also important to emphasize that the efficiency of the HPA is inversely related to the PAPR of the input signal, being given as [28]

$$\eta_{\mathrm{HPA}} = \left(\frac{1}{\mathrm{PAPR}}\right)^{\beta} \eta_{\mathrm{HPA}_{\max}}, \quad (19)$$

where $\eta_{\mathrm{HPA}_{\max}}$ is the maximal HPA efficiency and $\beta \in [0,1]$ is the efficiency exponent, which depends on the class of the HPA.

III. Benchmark Channel Estimators

The literature related to OTFS channel estimation usually involves estimating the channel characteristics in the DD domain. In this section, we present two well-established techniques, which we will denote as threshold channel estimation (TCE) [6] and correlation channel estimation (CCE) [7], to be used as performance benchmarks for our proposed LSTM-based channel estimator.

A. Threshold Channel Estimation (TCE)

The work in [6] is a seminal work for channel estimation in OTFS systems. The authors introduced an embedded pilot scheme, in which a sufficiently large guard interval is applied around a unique pilot to improve the acquisition of delay and

Doppler responses. As illustrated by Figure 2, the pilot and data symbols are allocated in the OTFS frame as

$$X_{\mathrm{DD}}[l,k]=\begin{cases}\text{pilots} & \text{if } l=l_p, k=k_p\\ 0 & \text{if } |l-l_p|\leq G_l, |k-k_p|\leq G_k\\ \text{data} & \text{otherwise}\end{cases}, \tag{20}$$

where G_l and G_k present the guard band along the delay and Doppler axis, respectively. Moreover, the pilot position (l_p,k_p) is known at the receiver side. This positioning of the pilot is strategic, allowing a simple channel estimation process by analyzing the received signal values around the DD grid of this embedded pilot. This guarantees that the receiver can segment the frame into one group comprising pilot and guard symbols, dedicated to channel estimation, and another group consisting of symbols for data detection. Such a structure ensures that received symbols designated for channel estimation do not interfere with those intended for data detection.

The channel estimation is based on the received symbols $\mathrm{Y}_{\mathrm{TCE}}[l,k]$ for the subgrid $(l_p-G_l\leq l\leq l_p+G_l, k_p-G_k\leq k\leq l_k+G_k)$. Thus, using the threshold method in which, for this grid, the estimated channel is given as

$$\hat{h}_{\mathrm{DD_{TCE}}}[l-l_p,k-k_p]=\begin{cases}\frac{Y_{\mathrm{TCE}}[l,k]}{X_{\mathrm{DD}}[l_p,k_p]}, & \text{if } Y_{\mathrm{TCE}}[l,k]\geq\vartheta\\ 0, & \text{otherwise}\end{cases}, \tag{21}$$

where ϑ is the detection threshold, which is arbitrarily fixed as $\vartheta=3\sigma_w$, with σ_w being the effective noise of the pilot signal. So, if there is a path, it can be seen on the receiver side as a scaled version of the pilot plus Gaussian noise [29]. Finally, the estimated channel is used for data detection.

B. Correlation Channel Estimation (CCE)

In [7], the authors propose an estimator for OTFS systems in which the cross-correlation channel matrix is acquired through estimation in the DD domain. As presented in Figure 3, they assume that the channel is invariant for more than one symbol duration, so the pilot and information are sent at different frames. Thus, the pilot signal in the DD domain is considered as

$$X_{\mathrm{DD}}[l,k]=\begin{cases}1 & \text{if } l=l_p, k=k_p\\ 0 & \text{otherwise}\end{cases}. \tag{22}$$

Thus, the estimated channel response in the DD domain can be written as

$$\begin{aligned}\hat{h}_{\mathrm{DD_{CCE}}}[l,k]=&\sum_{\mathrm{K}=1}^{\kappa}h_{\mathrm{K}}\delta\left((l-l_{\mathrm{K}})-l_{\tau_{\mathrm{K}}}\right)e^{j\phi_{\mathrm{K}}}\cdot\psi_{\mathrm{K}}[l]\\ &\times\Upsilon_N\left(k_{v_{\mathrm{K}}}+\kappa_{v_{\mathrm{K}}}-(k-k_{\mathrm{K}})\right)\end{aligned} \tag{23}$$

where h_{K} is the path gain, $l_{\tau_{\mathrm{K}}}$ and $k_{v_{\mathrm{K}}}$ represent the integer indices of the delay and the Doppler bins in the DD domain, respectively. The initial phase is represented as ϕ. The fractional Doppler is represented as $\kappa_{v_{\mathrm{K}}}$, which uses a noninteger index to represent the Doppler values for the $\mathrm{K}-$th, with $(k_{v_{\mathrm{K}}}+\kappa_{v_{\mathrm{K}}})$ being the DD representation of the path fractional Doppler. The phase shift due to the Doppler effect ψ_{K} and the function Υ_N are defined as

$$\psi_{\mathrm{K}}[l]\triangleq e^{j2\pi(k_{v_{\mathrm{K}}}+\kappa_{v_{\mathrm{K}}})\frac{N_{\mathrm{CP}}-l_{\tau_{\mathrm{K}}}+l}{(M+N_{\mathrm{CP}})N}} \tag{24}$$

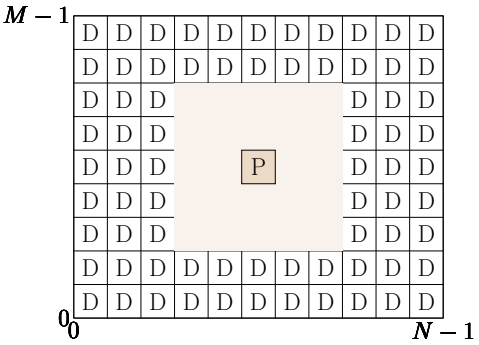

Fig. 2: DD domain frame structure for the TCE scheme proposed by [6], where D denotes the data resource elements and P the pilot, surrounded by the guard interval.

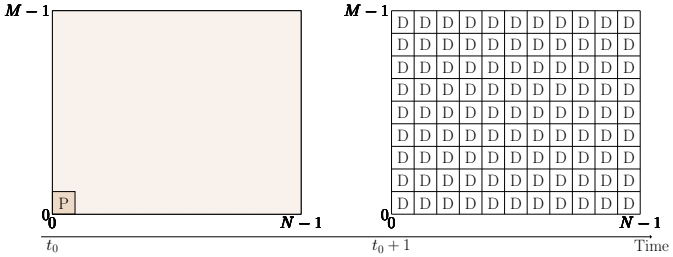

Fig. 3: DD domain frame structure for the CCE scheme proposed by [7], where the P pilot and the D data resource elements are sent at adjacent frames.

and

$$\Upsilon_N(x)\triangleq\sum_{n=1}^{N}e^{(j2\pi(n-1))\frac{x}{N}}, \tag{25}$$

where N_{CP} denotes the size of the cyclic prefix. Finally, this estimator is based on a cross-correlation function across Doppler delay elements, as detailed in [7].

While the CCE outperforms existing approaches in the literature, it does exhibit error floors under a high signal-to-noise ratio (SNR), which is a challenge for channel estimation in prospective OTFS applications. In addition, common to [6], [7] is that these works require a substantial guard interval to mitigate the interference of unknown data symbols in the pilots used for channel estimation. In addition, a high pilot SNR is required by the schemes proposed by [6], [7], which results in high signaling and pilot overheads to ensure accurate channel state information (CSI) estimation. As an important conclusion, these aspects can potentially negatively impact the PAPR of the transmitted signal, as highlighted in [12], and which can jeopardize their practical application.

IV. Proposed LSTM-Based Channel Estimator

In this section, we propose a new channel estimation scheme for OTFS systems subject to HPA-induced distortions. Our method starts with an initial channel estimate derived from the preamble and the frequency-domain pilots. This estimate serves as input to an LSTM layer, effectively tracking the channel's behavior. Subsequently, a shallow NN is applied to increase the denoising capability and refine the estimation

accuracy. Through these steps, we can maintain low pilot overhead and attain a reliable channel estimation, especially when dealing with nonlinear and highly selective channels.

We consider a basic transmitted packet consisting of a preamble with a known deterministic sequence, used for primary synchronization of the channel, followed by the data field. Moreover, the CP is used to absorb the inter-symbol interference (ISI) caused by the multi-path propagation. In the data field, M subcarriers are employed within each symbol, in which only $M_{\rm on}$ are active and the other are inactive subcarriers. In addition, considering the $M_{\rm on}$ subcarriers, $M_{\rm p}$ of them are allocated as pilots, while the remaining $M_{\rm d}$ subcarriers carry the data.

A. Signal Generation

In our proposal, the pilots are incorporated in the TF domain and, consequently, the number of subcarriers reserved for data transmission in the DD domain is decreased, while preserving the same subcarrier spacing and bandwidth. Let us first denote the set of active subcarriers as $\mathcal{M}_{\rm on}$, so that $M_{\rm on} = |\mathcal{M}_{\rm on}|$, while the set of pilot subcarriers is $\mathcal{M}_{\rm p}$, with $M_{\rm p} = |\mathcal{M}_{\rm p}|$. Our configuration results in a frame with $M_{\rm d}$ subcarriers dedicated to data that occupy the positions $\mathcal{M}_{\rm d}$ such that $\mathcal{M}_{\rm d} \cup \mathcal{M}_{\rm p} = \mathcal{M}_{\rm on}$. Then, we first transform $X_{\rm DD}$ to the TF domain, but only taking the data into account, obtaining the $M_{\rm d}$-by-N matrix

$$X_{\rm TF_d}[m_{\rm d}, n] = \frac{1}{\sqrt{N M_{\rm d}}} \sum_{k=0}^{N-1} \sum_{l=0}^{M_{\rm d}-1} X_{\rm DD}[l,k] e^{j2\pi\left(\frac{nk}{N} - \frac{m_{\rm d} l}{M_{\rm d}}\right)}, \tag{26}$$

in which $m_{\rm d} \in \mathcal{M}_{\rm d}$, and the pilot subcarriers are subsequently inserted by doing

$$X_{\rm TF}[m,n] = \begin{cases} \text{pilots} & \text{if } m \in \mathcal{M}_{\rm p} \\ X_{\rm TF_d}[m,n] & \text{if } m \in \mathcal{M}_{\rm d} \end{cases}. \tag{27}$$

Figure 4 illustrates the TF domain frame structure given in (27), in which the D represent the data subcarriers, obtained from (26), while P denotes the pilot subcarriers P. In addition, the preamble is shown as PR. Importantly, this configuration ensures that there is no overlap between the pilot and data subcarriers, optimizing the use of available resources in our estimation process.

B. Initial Estimation

We initiate our estimation process by utilizing the LS method for the preamble and pilot information in the frequency domain. The initial channel estimation in the preamble is obtained as

$$\hat{\rm H}_{\rm TF_{LS}}[m, n_{\rm pr}] = \frac{\rm Y[m, n_{\rm pr}]}{\mathcal{P}[m]}, \quad \forall m, \tag{28}$$

where $\rm Y[m, n_{\rm pr}]$ is the frequency domain signals for each m-th subcarrier, obtained by the demodulation of the training sequences from the preamble at the $n_{\rm pr}$ symbol position. Furthermore, $\mathcal{P}[m]$ represents the frequency domain predefined preamble sequence.

On the pilots' subcarriers, the initial channel estimation is obtained as

$$\hat{\rm H}_{\rm TF_{LS}}[m_{\rm p}, n] = \frac{\rm Y[m_{\rm p}, n]}{\rm S[m_{\rm p}, n]}, \quad \forall n. \tag{29}$$

Thus, for each n-th symbol, $\rm Y[m_{\rm p}, n]$ and $\rm S[m_{\rm p}, n]$ represent the frequency domain received and transmitted signals at the $m_{\rm p} \in \mathcal{M}_{\rm p}$ pilot positions, respectively. It should be noted here that, unlike the proposals in [6], [7], the pilots have the same power as the transmitted signal. Finally, to avoid interference in the training of the LSTM-NN network, which will be further explained, the information in the $M_{\rm d}$ data subcarriers is considered as null to build the initial channel estimation $\hat{\rm H}_{\rm TF_{LS}}[m, n]$. Consequently, the pilot information is used as a basis for interpolating the data carrier information and obtaining the final channel estimate.

C. LSTM Interpolation

We take advantage of the performance gain of the LSTM-based over traditional DNN-based receivers in symbol-by-symbol estimation [18], [30]. The LSTM is based on recurrent units to process and learn from a sequence of data [31], which is done by internal gate units capable of storing the memory content of the data while employing structures capable of deciding when to keep or override information of these memory cells. Unlike traditional feedforward DNN architectures, which may encounter challenges in effectively capturing long-term temporal dependencies in sequential data, LSTM efficiently learns the time correlations of the channel. It achieves this by leveraging its memory cell mechanism, allowing it to consider not only the current input but also the previous output when estimating the current output. Internally, the gates of the LSTM cell are calculated as [32]:

- Forget Gate: $f_t = \sigma(x_t U_f + h_{t-1} W_f + b_f)$
- Input Gate: $i_t = \sigma(x_t U_i + h_{t-1} W_i + b_i)$
- Output Gate: $o_t = \sigma(x_t U_o + h_{t-1} W_o + b_o)$

Here, σ denotes the activation function, where we favored the Rectified Linear Unit (ReLU) jointly with adaptive moment estimation (ADAM) as the optimizer. This preference is driven by its fast computing time, minimal parameter tuning requirements, and its well-established capability to address optimization problems effectively.

The weight matrices U_q, W_q correspond to the input and recurrent connections, where the subscript q can either be the input gate (i), output gate (o), or the forget gate (f). The notation h_{t-1} represents the previous hidden state and x_t the current input, while b_f, b_i, and b_o are bias terms. Thus, the behavior of an LSTM cell is guided by the following steps.

1) Internal Memory Update

$$c_t = \sigma(f_t \odot c_{t-1} + i_t \odot \widetilde{c}_t), \tag{30}$$

where $\widetilde{c}_t$ is the candidate memory state at time step t, which is calculated based on the current input and previous hidden state as

$$\widetilde{c}_t = \tanh(x_t U_c + h_{t-1} W_c + b_c), \tag{31}$$

where $\tanh$ denotes the hyperbolic tangent function, U_c and W_c represent the weight matrices corresponding to the input

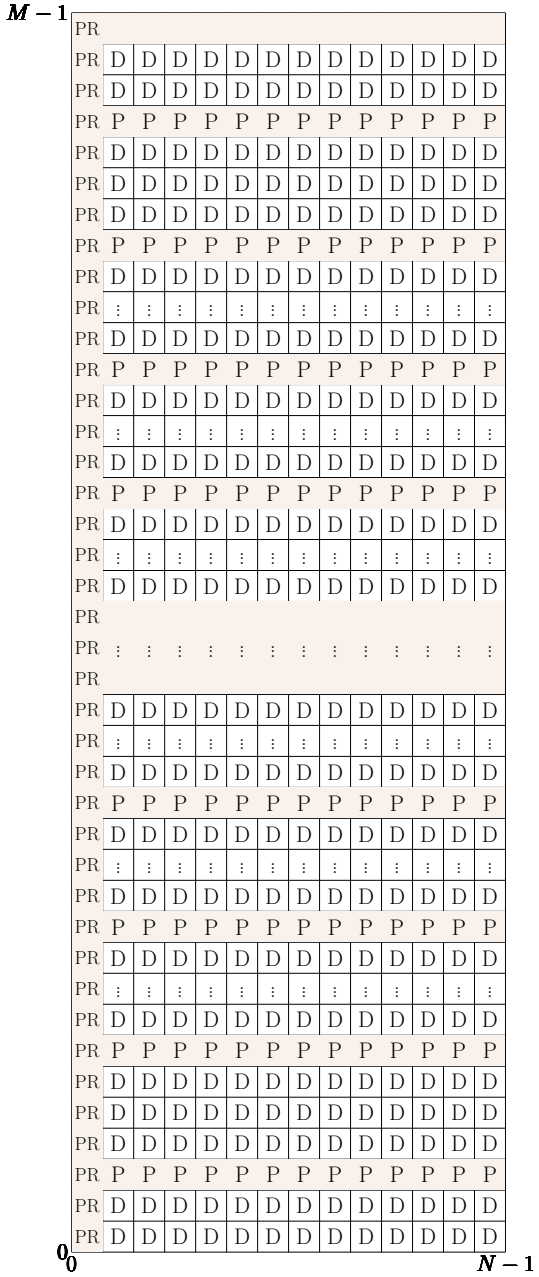

Fig. 4: TF domain frame structure for the proposed initial channel estimation. Here we denote the pilot subcarriers as P, the preamble as PR and D as the data subcarriers.

and recurrent connections, respectively, and b_c is the current bias for candidate memory information.

2) Hidden State Output Update

$$h_t = o_t \odot \tanh(c_t), \tag{32}$$

which is used for predictions or passed to the next time step.

In the context of channel estimation, I LSTM inputs must be used, which are related to the number of active subcarriers and pilot subcarriers. In addition, each LSTM network comprises χ hidden states, determining the number of steps t for the recurrent operations. Such processing characteristics of the LSTM allow it to learn the channel correlation over time and adapt the channel estimates accordingly. Thus, we consider the initial channel estimation presented in Subsection IV-B as the initial point to perform LSTM-based interpolation for the data positions and obtain the channel information for the entire frame.

D. NN Noise Compensation

Aiming to reduce the noise, the output of the LSTM layer is further processed by a shallow NN with ω neurons. The goal of the LSTM-NN network is to update the estimation initially obtained and learn to correct the estimation errors compared to the channel with perfect CSI. We follow the methodology outlined in [33] to establish the parameters for both the training and testing phases of our approach. The dataset is split into training and testing sets by randomly selecting 80% and 20%, respectively, from a pool of $10{,}000$ distinct realizations of the vehicular channel. The batch size is set to be sufficiently smaller than the size of the training dataset, facilitating faster generalization and training. The number of training epochs is carefully selected to ensure model convergence. For optimization, we adopt the ADAM optimizer paired with the ReLU activation function to minimize the loss between the perfect channel and the estimates produced by the LS-LSTM-NN architecture. Following recommendations from [33], we set the learning rate to 0.001, allowing ADAM to adapt dynamically throughout training until convergence is achieved. The NN network is trained to determine the parameter $\theta^\star$ that minimizes the loss function ℓ, which measures the approximation

$$\theta^\star = \underset{\theta}{\operatorname{argmin}}\ \ell\left(\theta, \hat{\mathrm{H}}_{\mathrm{TF}_{\mathrm{LSTM}}}[m,n], \mathrm{H}_{\mathrm{TF}}[m,n]\right), \tag{33}$$

where θ represents the NN weight vector, $\mathrm{H}_{\mathrm{TF}}[m,n]$ is the perfect channel response obtained from the vector of training samples, used during the training stage of the proposed estimator, while $\hat{\mathrm{H}}_{\mathrm{TF}_{\mathrm{LSTM}}}[m,n]$ is the output of the LSTM.

The loss is evaluated as

$$\ell\left(\theta, \hat{\mathrm{H}}_{\mathrm{TF}_{\mathrm{LSTM}}}[m,n], \mathrm{H}_{\mathrm{TF}}[m,n]\right) = \frac{1}{NM}\sum_{m=0}^{M-1}\sum_{n=0}^{N-1}\left|\mathrm{H}_{\mathrm{TF}}[m,n] - \hat{f}\left(\hat{\mathrm{H}}_{\mathrm{TF}_{\mathrm{LSTM}}}[m,n];\theta\right)\right|^2, \tag{34}$$

where $\hat{f}\left(\hat{\mathrm{H}}_{\mathrm{TF}_{\mathrm{LSTM}}}[m,n];\theta\right)$ is the output of the NN, represented as a function of LSTM estimate $\hat{\mathrm{H}}_{\mathrm{TF}_{\mathrm{LSTM}}}$.

Notice that this process during the training stage is iterative, with the LSTM-NN network adapting $\hat{f}\left(\hat{\mathrm{H}}_{\mathrm{TF}_{\mathrm{LSTM}}}[m,n];\theta\right)$ given each training sample. Finally, the final channel estimation is obtained as

$$\hat{\mathrm{H}}_{\mathrm{LS-LSTM-NN}}[m,n] = \hat{f}\left(\hat{\mathrm{H}}_{\mathrm{TF}_{\mathrm{LSTM}}}[m,n];\theta^\star\right). \tag{35}$$

Figure 5 shows the block diagram of the proposed LS-LSTM-NN channel estimator for OTFS systems, while Table I summarizes the DL architecture and parameters used in the training phase from our proposed scheme. Combining the initial estimate, LSTM, and NN provides a reliable estimation of

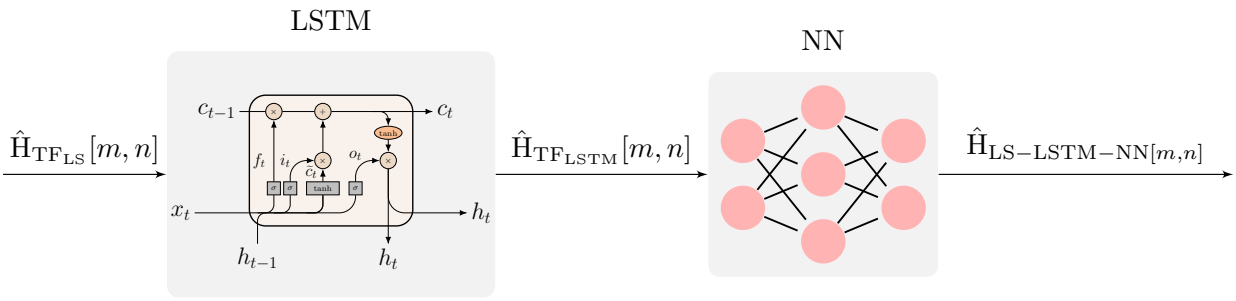

Fig. 5: Block diagram of the proposed LS-LSTM-NN estimator.

TABLE I: Parameters for training the proposed estimator.

Parameter	Values
Hidden size of the LSTM	χ
Hidden size of the NN	ω
Training samples	8000
Testing samples	2000
Batch size	128
Epochs	500
Optimizer	Adam
Learning rate	0.001

TABLE II: Simulation parameters.

Parameter	Values
Bandwidth (B)	10 MHz
Carrier Frequency (f_c)	5.9 GHz
Symbol Duration (T)	8 μs
Number of symbols (N)	14
Number of subcarriers (M)	64
Subcarrier spacing	156.25 KHz
Speed (v)	$\{300\}$ km/h
IBO	$\{2, 4\}$ dB
Modulations	QPSK, 16-QAM

the channel with unknown instantaneous variation. In addition, the use of multiple pilot symbols is advantageous due to a substantial reduction in the PAPR of OTFS signals. Notably, this approach aligns with practical scenarios characterized by nonlinearities [12]. Also importantly, our analysis shows that this achievement does not compromise the spectral efficiency. In fact, our proposed solution achieves nearly optimal performance in this regard, reinforcing the effectiveness of our approach.

V. Simulation Results

In this section, we conduct a comparative analysis to evaluate the performance of the LS-LSTM-NN receiver, outlined in Section IV, within a scenario affected by distortions resulting from HPA nonlinearities. The performance evaluation scheme is done in terms of BER, throughput, PAPR, and computational complexity. We compare our proposal with the benchmark methods TCE [6] and CCE [7], in which channel estimation is done using the pilot response in the delay-Doppler domain. For both benchmark methods, the SNR for the pilots is assumed to be $\mathrm{SNR_p} = 40$ dB, as per their design. To support reproducibility, the codes used for the simulated results can be downloaded at [34].

To ensure compatibility, our system is inspired by the physical layer specifications of the IEEE 802.11p [35] communication standard. Thereby, we consider a bandwidth of $B = 10$ MHz, with a carrier frequency of $f_c = 5.9$ GHz to transmit a frame with $M = 64$ subcarriers and $N = 14$ symbols. Furthermore, we account for turbo LTE coding with a rate of $1/2$ and utilize the MMSE criterion for equalization. It is also important to note that, unlike the other estimators, our proposed method conducts the equalization process within the TF domain[1]. The results show the performances in a scenario considering the ITU-T Vehicular-A [36] with speed $v = 300$ km/h and [16-QAM, QPSK] modulation orders. Furthermore, our evaluation takes into consideration the impact of HPA nonlinearities considering an IBO $= 4$ dB for the highest modulation order and IBO $= 2$ dB for the nonlinear effects on QPSK modulation. Table II summarizes the simulation parameters.

A. BER

To evaluate the detection capabilities of the different methods in a scenario that includes the nonlinearities induced by HPAs, this section explores the BER of the transmitted signals.

Figure 6 compares the BER of the channel estimation methods in a scenario involving QPSK modulation and IBO $=$ 2 dB. As shown, the estimators perform similarly at low SNR. Nevertheless, as the SNR increases over 20 dB, an error floor becomes evident in the benchmark estimators. In contrast, the LS-LSTM-NN estimator is the best performer, closely approaching the detection performance when perfect CSI is considered. Remarkably, even with an elevated SNR level of 30 dB, our estimator is the only one capable of achieving a BER below 10^{-3}, presenting a gain of at least 5 dB for this particular error rate threshold, compared to [6], [7].

Figure 7 evaluates the BER performance considering a 16-QAM modulation and IBO $= 4$ dB. Similarly to the results observed in QPSK modulation, at low SNR the considered channel estimators exhibit comparable performances. However, a notable gain is observed for the proposed method in

[1]During our evaluations across the different scenarios, we found that conducting DD equalization within the channel estimated with our method led to detection results similar to those in the TF domain, but with increased computational complexity.

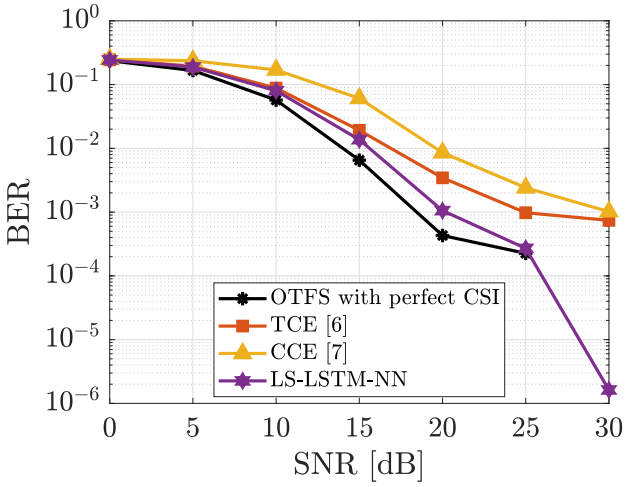

Fig. 6: BER analysis for $v = 300$ km/h and QPSK modulation and IBO $= 2$ dB.

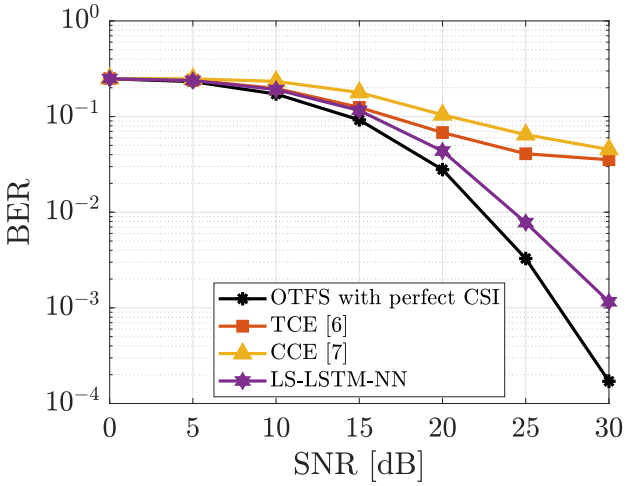

Fig. 7: BER analysis for $v = 300$ km/h and 16-QAM modulation and IBO $= 4$ dB.

the high SNR region. Furthermore, both estimators presented in [6] and [7] show an even more expressive error floor at high SNR for scenarios with higher modulation order. Consequently, these estimators fail to reduce the BER to a level lower than 10^{-2} during signal detection.

The PAPR analysis in Section V-C will further explore this result. Higher modulation orders yield greater variations in the amplitude of the transmitted signal, which significantly affects the detection of benchmark estimators. In this sense, we remark that the increased performance of the proposed LS-LSTM-NN is evident, as it is the only one capable of achieving an error rate of 10^{-3} and, therefore, is the sole one to provide reliable channel estimates in such scenarios.

B. Throughput

Complementing the BER analysis of the previous section, we now compare the channel estimators in terms of system throughput. Our proposed estimator operates within a frame

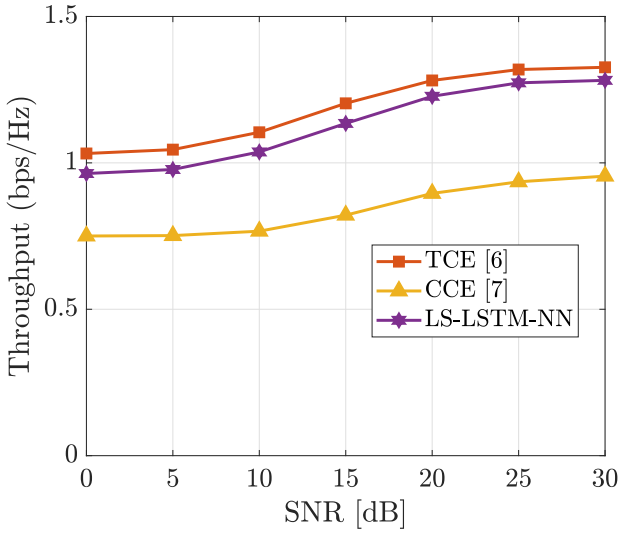

Fig. 8: Throughput analysis for $v = 300$ km/h, 16-QAM modulation and IBO $= 4$ dB.

structure where $M_{\mathrm{p}} = 8$ subcarriers are designated as pilots in the frequency domain. Meanwhile, $M_{\mathrm{d}} = 44$ subcarriers carry data, and the additional 12 subcarriers act as a guard band. Moreover, these symbols are preceded by a unique preamble. Thus, the data density of the transmitted frame can be written as

$$\rho_{\mathrm{LS-LSTM-NN}} = \frac{NM_{\mathrm{d}}}{(N+1)\,M} \approx 64\%. \tag{36}$$

To ensure a fair comparison, we consider that the channel estimator proposed by [6] takes into account a frame with a single pilot inserted in the DD domain that is surrounded by a guard band that achieves a data density similar to our proposal, except for the preamble. Thus,

$$\rho_{\mathrm{TCE}} = \frac{NM_{\mathrm{d}}}{NM} \approx 69\%. \tag{37}$$

In contrast, since the estimator introduced in [7] adopts an arrangement where pilot and data transmissions are transmitted in separate frames, as depicted in Figure 3, this design leads to a spectral efficiency of

$$\rho_{\mathrm{CCE}} = 50\%, \tag{38}$$

which will mark a reduction in the data density compared to the TCE method and the proposed LS-LSTM-NN scheme. Thus, we analyze this loss by comparing the throughput of the transmission, calculated as [37]

$$T_i = \rho_i \; r \; (1 - \mathrm{BER}_i), \tag{39}$$

where the index i is used to differentiate the channel estimation schemes and r is the modulation and coding scheme (MCS) average factor.

Figure 8 presents the throughput comparison for the different estimators, considering $N = 14$ symbols, $v = 300$ km/h, 16-QAM modulation, and IBO $= 4$ dB. As illustrated, the estimator proposed in [6] is the one that offers the best performance in terms of throughput, which is mainly due to

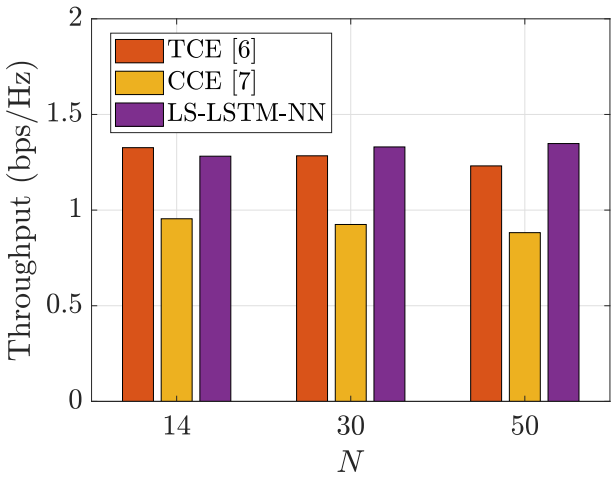

Fig. 9: Throughput analysis for $v = 300$ km/h, 16-QAM modulation, IBO $= 4$ dB, and SNR $= 30$ dB for different frame sizes.

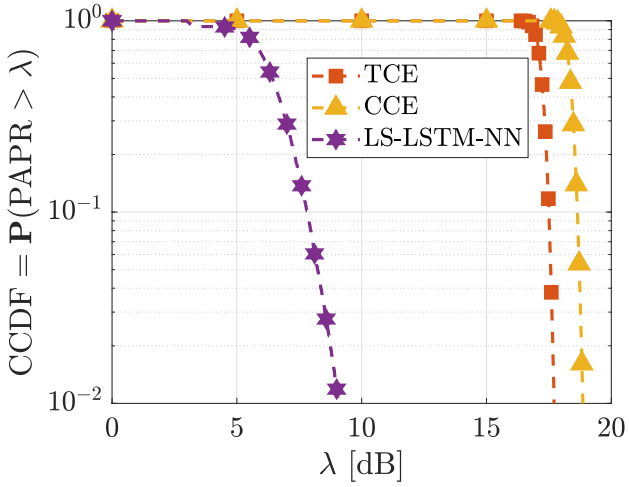

Fig. 10: PAPR analysis.

the choice of the guard band to define the spectral efficiency in (37). However, our proposed estimator closely approaches this benchmark while outperforming the method introduced by [7]. Moreover, it is important to highlight that the slight reduction in the throughput of our approach is counterbalanced with substantial enhancements in terms of BER, as illustrated by Figure 7. An additional investigation of the throughput in the same scenario, but with a fixed SNR of 30 dB and different frame sizes N, presented in Figure 9, reveals an important trend. Our proposed solution exhibits improved performance as the block size increases, which is expected due to the use of a unique preamble. For instance, when the frame size is $N \geq 30$ symbols, the proposed LS-LSTM-NN scheme outperforms [6], [7] in terms of throughput.

C. PAPR

The PAPR analysis holds critical significance within real-world communications scenarios. In this subsection, we compare the channel estimation techniques in terms of their impact on the CCDF, which is often employed to assess signal PAPR distortion and provides insights into the probability of signal exceeding a given power level λ.

The CCDF analysis comparing the different estimators is illustrated in Figure 10. As we observe in the figure, the comparison between the estimators highlights the problem of allocating pilots with very high power to facilitate channel estimation in the DD domain. Specifically, the proposed LS-LSTM-NN estimator yields a PAPR threshold gain of at least 8 dB when compared with the method proposed in [6]. Moreover, this advantage is even more pronounced when compared to the estimator presented in [7]. This result underscores the significant impact on channel estimation accuracy from the benchmarks, primarily due to the reliance on a much higher pilot power compared to the average power of a transmission frame, resulting in elevated PAPR levels [11]. Consequently, the requirement for high pilot overhead can lead to inefficient resource utilization, which may adversely impact power efficiency [17]. In this context, TF domain pilot positions offer more efficient utilization of resources compared to DD domain pilot placements.

Let us remark that determining an acceptable PAPR threshold depends on several factors, including the specific attributes of the communication system, the characteristics of the HPA, and the performance requirements of the application. Additionally, we point out that the PAPR limitation due to high power pilots in the DD domain is a factor already investigated in the existing literature [12]. Nevertheless, maintaining a lower PAPR holds paramount importance in mitigating the distortion induced by HPAs. This importance arises from the indication that the efficiency of HPA decreases with the increase of the PAPR of the input signal, as notable in (19). Indeed, it is worth noting that higher PAPR values can significantly jeopardize the quality of communication and are generally impractical in real-world scenarios [9]. In contrast, our scheme offers a practical avenue for OTFS communication.

D. Computational Complexity

To assess the computational complexity of the schemes, we quantify the complexity order of the operations needed to estimate the channel from a received symbol. The channel estimation algorithm in [6] requires comparing N symbols and the maximum Doppler samples with a given threshold, which yields a complexity order of $\mathcal{O}(N\,M)$. In addition, this method depends on the equalization in the DD domain, which is significantly complex due to the need to invert the channel matrix. The complexity of the MMSE equalization in the DD domain is of order $\mathcal{O}(M_{\mathrm{d}}^3\,N^3)$ [26]. Thus, the complexity order of the TCE scheme is given by

$$\mathcal{C}_{\mathrm{TCE}} = \mathcal{O}(N\,M + M_{\mathrm{d}}^3\,N^3). \tag{40}$$

By its turn, the estimation algorithm in [7] uses the FFT for correlation operations, while equalization is also performed in the DD domain, thus having a complexity order of

$$\mathcal{C}_{\mathrm{CCE}} = \mathcal{O}(\kappa\,D\,M\,N\log N + M_{\mathrm{d}}^3\,N^3), \tag{41}$$

TABLE III: Computational complexity.

Method	Computational Complexity
TCE [6]	$\mathcal{O}(MN + M_{\mathrm{d}}^3 N^3)$
CCE [7]	$\mathcal{O}(\kappa DMN \log N + M_{\mathrm{d}}^3 N^3)$
LS-LSTM-NN	$\mathcal{O}(M_{\mathrm{on}}^2 + M_{\mathrm{p}}^2 + M_{\mathrm{on}} M_{\mathrm{p}} + M_{\mathrm{d}}\, N)$

where D is the resolution of the fractional Doppler, while κ is the number of paths of the vehicular channel, which in the case of Vehicular A model is $\kappa = 9$ [36].

The proposed LS-LSTM-NN estimator employs the LS initial estimation, with the number of operations required being

$$C_{\mathrm{LS}} = 2\, M_{\mathrm{on}}. \tag{42}$$

Such initial estimation is followed by the LSTM unit with computational complexity depending on the input size, here denoted as $I = M_{\mathrm{d}} + M_{\mathrm{p}}$, and the size of its hidden states $\chi = \frac{M_{\mathrm{d}}+M_{\mathrm{p}}}{2}$. The overall number of operations of the LSTM unit is given by [18]

$$\begin{aligned} C_{\mathrm{LSTM}} &= 4\chi^2 + 4\chi\, I + 3\chi \\ &= 3M_{\mathrm{d}}^2 + 3M_{\mathrm{p}}^2 + 6M_{\mathrm{d}}M_{\mathrm{p}} + 3\frac{M_{\mathrm{d}} + M_{\mathrm{p}}}{2}. \end{aligned} \tag{43}$$

The shallow NN has a single hidden layer with $\omega = 15$ neurons and $\omega_{\mathrm{in}} = \omega_{\mathrm{out}} = 2M_{\mathrm{on}}$ input and output layers. Thus, its computational complexity is given by

$$C_{\mathrm{NN}} = 15\omega_{\mathrm{in}} + 15\,\omega_{\mathrm{out}} = 60M_{\mathrm{on}}. \tag{44}$$

Therefore, the order of the computational complexity of the LS-LSTM-NN estimator can be written as $\mathcal{O}(M_{\mathrm{on}}^2 + M_{\mathrm{p}}^2 + M_{\mathrm{on}}M_{\mathrm{p}})$.

Differently from [6], [7], the LS-LSTM-NN estimator performs equalization in the TF domain. This decision is motivated by practical considerations to manage the complexity of the receiver. Research findings, such as those in reference [38], indicate that DD domain processing can introduce a higher degree of complexity. The complexity order of the MMSE equalization in the TF domain is $\mathcal{O}(M_{\mathrm{d}}\, N)$ [26]. Combining the above, we have that

$$\mathcal{C}_{\mathrm{LS-LSTM-NN}} = \mathcal{O}(M_{\mathrm{on}}^2 + M_{\mathrm{p}}^2 + M_{\mathrm{on}} M_{\mathrm{p}} + M_{\mathrm{d}}\, N). \tag{45}$$

Table III summarizes the complexity order required for each method compared in this paper to detect the transmitted signal. In Figure 11, the order of the computational complexity is calculated over different frame sizes, clearly emphasizing the reduction in complexity achieved by the proposed LS-LSTM-NN channel estimator, independently of the chosen N.

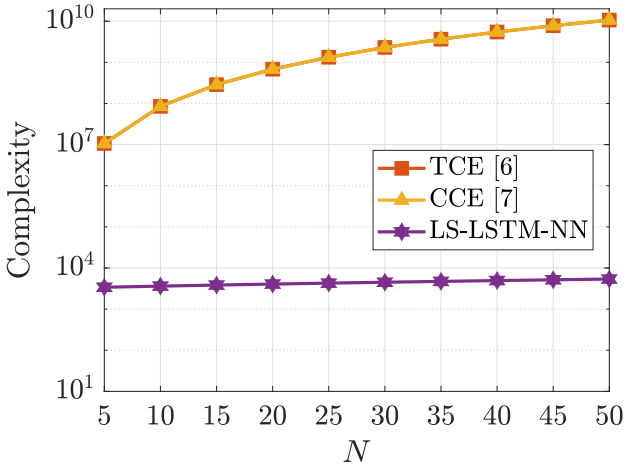

Fig. 11: Computational complexity for different frame sizes.

VI. Conclusion

This work is focused on addressing the challenge of channel estimation in OTFS communication systems while considering the nonlinear effects induced by HPAs. In this context, we present an alternative strategy to face the conventional methods where channel estimation is based on high-power pilot subcarriers inserted in the delay-Doppler domain, leading to elevated PAPR levels and compromising system performance. Our proposed LS-LSTM-NN estimator is based on a time-frequency domain pilot insertion scheme, effectively mitigating PAPR-related issues without sacrificing system throughput. Furthermore, our approach exhibited significant robustness against HPA-induced nonlinearities, as evidenced by the BER and PAPR evaluations conducted under different modulation schemes and SNR conditions. Remarkably, our method significantly reduces the computational complexity during signal detection, making it more suitable for future real-world applications.

References

[1] D. C. Nguyen, M. Ding, P. N. Pathirana, A. Seneviratne, J. Li, D. Niyato, O. Dobre, and H. V. Poor, "6G internet of things: A comprehensive survey," *IEEE Internet of Things Journal*, vol. 9, no. 1, pp. 359–383, 2022.

[2] Z. Wei, W. Yuan, S. Li, J. Yuan, G. Bharatula, R. Hadani, and L. Hanzo, "Orthogonal time-frequency space modulation: A promising next-generation waveform," *IEEE Wireless Communications*, vol. 28, no. 4, pp. 136–144, 2021.

[3] Z. Wei, S. Li, W. Yuan, R. Schober, and G. Caire, "Orthogonal time frequency space modulation—part I: Fundamentals and challenges ahead," *IEEE Communications Letters*, vol. 27, no. 1, pp. 4–8, 2023.

[4] R. Hadani, S. Rakib, M. Tsatsanis, A. Monk, A. J. Goldsmith, A. F. Molisch, and R. Calderbank, "Orthogonal time frequency space modulation," in *2017 IEEE Wireless Communications and Networaking Conference (WCNC)*, 2017, pp. 1–6.

[5] R. Hadani and A. Monk, "OTFS: A new generation of modulation addressing the challenges of 5G," 2018. [Online]. Available: https://arxiv.org/pdf/1802.0262.

[6] P. Raviteja, K. T. Phan, and Y. Hong, "Embedded pilot-aided channel estimation for OTFS in delay–doppler channels," *IEEE Transactions on Vehicular Technology*, vol. 68, no. 5, pp. 4906–4917, 2019.

[7] N. Hashimoto, N. Osawa, K. Yamazaki, and S. Ibi, "Channel estimation and equalization for CP-OFDM-based OTFS in fractional doppler channels," in *2021 IEEE International Conference on Communications Workshops (ICC Workshops)*, 2021, pp. 1–7.

[8] G. D. Surabhi, R. M. Augustine, and A. Chockalingam, "Peak-to-average power ratio of OTFS modulation," *IEEE Communications Letters*, vol. 23, no. 6, pp. 999–1002, 2019.

[9] S. Gao and J. Zheng, "Peak-to-average power ratio reduction in pilot-embedded OTFS modulation through iterative clipping and filtering," *IEEE Communications Letters*, vol. 24, no. 9, pp. 2055–2059, 2020.

[10] C. Naveen and V. Sudha, "Peak-to-average power ratio reduction in OTFS modulation using companding technique," in *2020 5th International Conference on Devices, Circuits and Systems (ICDCS)*, 2020, pp. 140–143.
[11] H.-T. Sheng and W.-R. Wu, "Time-frequency domain channel estimation for OTFS systems," *IEEE Transactions on Wireless Communications*, vol. 23, no. 2, pp. 937–948, 2024.
[12] R. Marsalek, J. Blumenstein, A. Prokes, and T. Gotthans, "Orthogonal time frequency space modulation: Pilot power allocation and nonlinear power amplifiers," in *2019 IEEE International Symposium on Signal Processing and Information Technology (ISSPIT)*, 2019, pp. 1–4.
[13] H. Ye, G. Y. Li, and B.-H. Juang, "Power of deep learning for channel estimation and signal detection in OFDM systems," *IEEE Wireless Communications Letters*, vol. 7, no. 1, pp. 114–117, 2017.
[14] Y. Wu, C. Han, and Z. Chen, "DFT-spread orthogonal time frequency space system with superimposed pilots for terahertz integrated sensing and communication," *IEEE Transactions on Wireless Communications*, vol. 22, no. 11, pp. 7361–7376, 2023.
[15] M. Liu, M.-M. Zhao, M. Lei, and M.-J. Zhao, "Autoencoder based papr reduction for OTFS modulation," in *2021 IEEE 94th Vehicular Technology Conference (VTC2021-Fall)*. IEEE, 2021, pp. 1–5.
[16] S. Srivastava, R. K. Singh, A. K. Jagannatham, and L. Hanzo, "Bayesian learning aided sparse channel estimation for orthogonal time frequency space modulated systems," *IEEE Transactions on Vehicular Technology*, vol. 70, no. 8, pp. 8343–8348, 2021.
[17] H. Zhang, X. Huang, and J. A. Zhang, "Low-overhead OTFS transmission with frequency or time domain channel estimation," *IEEE Transactions on Vehicular Technology*, vol. 73, no. 1, pp. 799–811, 2024.
[18] A. F. Dos Reis, Y. Medjahdi, B. S. Chang, J. Sublime, G. Brante, and C. F. Bader, "Low complexity LSTM-NN-based receiver for vehicular communications in the presence of high-power amplifier distortions," *IEEE Access*, vol. 10, pp. 121 985–122 000, 2022.
[19] H. Shaiek, R. Zayani, Y. Medjahdi, and D. Roviras, "Analytical analysis of SER for beyond 5G post-OFDM waveforms in presence of high power amplifiers," *IEEE Access*, vol. 7, pp. 29 441–29 452, 2019.
[20] R4-163314, "Realistic power amplifier model for the new radio evaluation," 3GPP TSG-RAN WG4 Meeting, Tech. Rep., 2016.
[21] L. Rugini and P. Banelli, "BER of OFDM systems impaired by carrier frequency offset in multipath fading channels," *IEEE Transactions on Wireless Communications*, vol. 4, no. 5, pp. 2279–2288, 2005.
[22] J. J. Bussgang, *Crosscorrelation functions of amplitude-distorted Gaussian signals*. Res. Lab. of Electronics, MIT, Cambridge, MA., USA, Tech. Rep. 216, 1952.
[23] P. Colantonio, F. Giannini, and E. Limiti, *High efficiency RF and microwave solid state power amplifiers*. John Wiley & Sons, 2009.
[24] P. Raviteja, K. T. Phan, Y. Hong, and E. Viterbo, "Interference cancellation and iterative detection for orthogonal time frequency space modulation," *IEEE Transactions on Wireless Communications*, vol. 17, no. 10, pp. 6501–6515, 2018.
[25] P. Raviteja, Y. Hong, E. Viterbo, and E. Biglieri, "Practical pulse-shaping waveforms for reduced-cyclic-prefix OTFS," *IEEE Transactions on Vehicular Technology*, vol. 68, no. 1, pp. 957–961, 2019.
[26] R. P. Junior, C. A. F. da Rocha, B. S. Chang, and D. Le Ruyet, "A two-dimensional FFT precoded filter bank scheme," *IEEE Transactions on Wireless Communications*, vol. 22, no. 11, pp. 8366–8377, 2023.
[27] X. Xu, P. Yang, B. Zhang, Y. Xiao, and S. Li, "An improved PAPR reduction method based on imperialist competition algorithm for OTFS system," in *2022 IEEE 96th Vehicular Technology Conference (VTC2022-Fall)*, 2022, pp. 1–6.
[28] I. Ajayi, Y. Medjahdi, L. Mroueh, R. Zayani, and F. Kaddour, "Secrecy energy efficiency in PAPR-aware artificial noise scheme for secure massive MIMO," in *2023 Joint European Conference on Networks and Communications 6G Summit (EuCNC/6G Summit)*, 2023, pp. 42–47.
[29] A. Naikoti and A. Chockalingam, "Signal detection and channel estimation in OTFS," *ZTE Communications*, vol. 19, no. 4, pp. 16–33, 2021.
[30] A. K. Gizzini and M. Chafii, "A survey on deep learning based channel estimation in doubly dispersive environments," *IEEE Access*, vol. 10, pp. 70 595–70 619, 2022.
[31] S. Hochreiter and J. Schmidhuber, "Long short-term memory," *Neural computation*, vol. 9, no. 8, pp. 1735–1780, 1997.
[32] T. Ergen and S. S. Kozat, "Unsupervised anomaly detection with LSTM neural networks," *IEEE Transactions on Neural Networks and Learning Systems*, vol. 31, no. 8, pp. 3127–3141, 2020.
[33] I. Goodfellow, Y. Bengio, and A. Courville, *Deep learning*. MIT press, 2016.
[34] A. F. Dos Reis, "LSTM-based channel estimation for OTFS modulation." [Online]. Available: https://github.com/anafreis/OTFS_CE
[35] IEEE Standard Association, "IEEE guide for wireless access in vehicular environments (WAVE) architecture," *IEEE Std 1609.0-2013*, pp. 1–78, 2014.
[36] E. U. T. R. Access, "Base station (BS) radio transmission and reception," *ETSI, TS*, vol. 136, no. 104, p. V8, 2009.
[37] T. Shafique, M. Zia, H.-D. Han, and H. Mahmood, "Cross-layer chase combining with selective retransmission, analysis, and throughput optimization for OFDM systems," *IEEE Transactions on Communications*, vol. 64, no. 6, pp. 2311–2325, 2016.
[38] S. S. Das, V. Rangamgari, S. Tiwari, and S. C. Mondal, "Time domain channel estimation and equalization of CP-OTFS under multiple fractional dopplers and residual synchronization errors," *IEEE Access*, vol. 9, pp. 10 561–10 576, 2021.